Chemical Science

ROYAL SOCIETY OF CHEMISTRY

EDGE ARTICLE

View Article Online
View Journal | View Issue

Cite this: *Chem. Sci.*, 2025, **16**, 18190

All publication charges for this article have been paid for by the Royal Society of Chemistry

Acid vapor-induced enhanced electrical current rectification in phenothiazine-based electronic devices

Reshma Kumari, †[a] Nila Pal,†[b] Rajwinder Kaur,[b] Gunjan,[a] Ritika Sharma,[a] Debashree Manna,[c] Konstantin Katin,[d] Prakash Chandra Mondal *[b] and Marilyn Daisy Milton *[a]

Received 27th May 2025
Accepted 27th August 2025

DOI: 10.1039/d5sc03848k

rsc.li/chemical-science

Engineering transformable electronic features in two-terminal molecular junctions is of significant interest for advancing molecular-scale electronics. We demonstrate external stimuli (acid vapor)-responsive enhanced electrical current rectification (so called diode) in phenothiazine-based (**R1**) vertically stacked molecular junctions (MJs) with a configuration of p^+-Si/$\mathbf{R1}_{58\ nm}$/ITO. The fabricated junctions exhibit nearly 530% enhancement in the electrical current rectification ratio (RR) in response to acid-vapor exposure for 60 seconds. The electronic functions of the devices can be partially set back using triethylamine (a weak base) vapor. Exposure to acid vapor forms cation radicals, $(\mathbf{R1}^{\bullet+})\mathbf{H}^+$, that bring the lowest unoccupied molecular orbital (LUMO) closer to the Fermi level (E_F) of the ITO electrode in forward bias. In contrast, alignment of the highest occupied molecular orbital (HOMO) is not favorable under reverse bias conditions, which causes the emergence of the rectification ratio in the acid-exposed MJs. Electrical impedance spectra reveal a high charge transfer resistance (R_{ct}) of about 6 MΩ in pristine MJs, behaving like a resistor. However, the acid vapor facilitates an enhanced current flow at the forward bias compared to that at the reverse bias, mimicking diode functionality. The molecular junctions scrutinized for alternating current (AC) to direct current (DC) conversion using a function generator exhibit optimal diode performance at 500 Hz. Our findings demonstrate a method for high-yield device fabrication (~86% working devices) that can be utilized for acid- and base-vapor-facilitated transformable electronic functions mimicking traditional electronics.

Introduction

Realizing various electronic components such as switches, wires, transistors, diodes, negative differential resistance devices, and memristors using nanoscale molecular junctions (MJs) is crucial for mimicking the complementary metal-oxide semiconductor (CMOS) technology.[1,2] An MJ is a replica of conventional electronic devices where either a single molecule or an assembly of many molecules, such as organic molecules, metal complexes, and biomolecules, is sandwiched between two macroscopic electrical contacts for investigating electrical properties, a current–voltage (*I*–*V*) characteristic.[3–7] An *I*–*V* characteristic of an MJ in response to an applied external bias, varied molecular layer thickness, and external factors including the electric field, the magnetic field, and temperature facilitates our understanding on the underlying charge transport mechanism of diverse electronic functions originating in the MJs.[8–16] The key aspect of molecular electronics (MEs) is to study and analyze *I*–*V* response by varying molecular structures, thicknesses, compositions, device architectures, and electrodes.[17–24] Achieving stimuli-responsive, reversible electronic functions has been a long-standing goal of molecular electronics.[25–28] The electrical current rectification property observed in MJs is attributed to the asymmetry in either molecular structures (donor–acceptor), electrode compositions, or alignment of the frontier molecular orbitals at opposite bias polarity.[29–33] External chemical stimuli can either induce or enhance the current rectification of a MJ. For instance, humidity- and pH-controlled molecular rectifying junctions have been documented.[25,26,34,35] The electrical current rectification ratio (RR) in an electronic device can be defined as $\mathrm{RR} = \left|\frac{J(+V)}{J(-V)}\right|$, where $J(+V), J(-V)$ indicate current densities (Amp per cm^2) at specific positive and negative biases applied to the electrodes of the junctions. Since Aviram and Ratner's first

[a]*Functional Organic Molecules Synthesis Laboratory, Department of Chemistry, University of Delhi, Delhi-110 007, India. E-mail: mdmilton@chemistry.du.ac.in*

[b]*Department of Chemistry, Indian Institute of Technology Kanpur, Uttar Pradesh-208016, India. E-mail: pcmondal@iitk.ac.in*

[c]*Institute of Organic Chemistry and Biochemistry, Czech Academy of Sciences, Flemingovo náměstí 542/2, 160 00 Prague, Czech Republic*

[d]*Institute of Nanotechnologies in Electronics, Spintronics and Photonics, National Research Nuclear University "MEPhI", Moscow 115409, Russia*

† These authors contributed equally to this work.

theoretical work on molecular rectification in 1974, many organic molecules containing donor–π–acceptor (D–π–A) skeletons have been incorporated into electronic devices as circuit elements for realizing diode functionality.[36,37] Spatially asymmetric D–π–A systems are expected to show high conductance in forward bias due to favorable charge transport from the donor to the acceptor moiety, while less current flows at reverse bias polarity.

Organic molecules that show fluorescence changes in solution have been known for a long time and potentially deployed in molecular logic gates. Several groups, including Uchiyama, de Silva, McCoy, and Magri, introduced the concept of molecular logic gates, and the field was advanced with either chemicals or light for luminescence-based sensor applications.[38–43] One of the design strategies that includes switchable fluorescent organic materials is based on donor–π–acceptor (D–π–A)

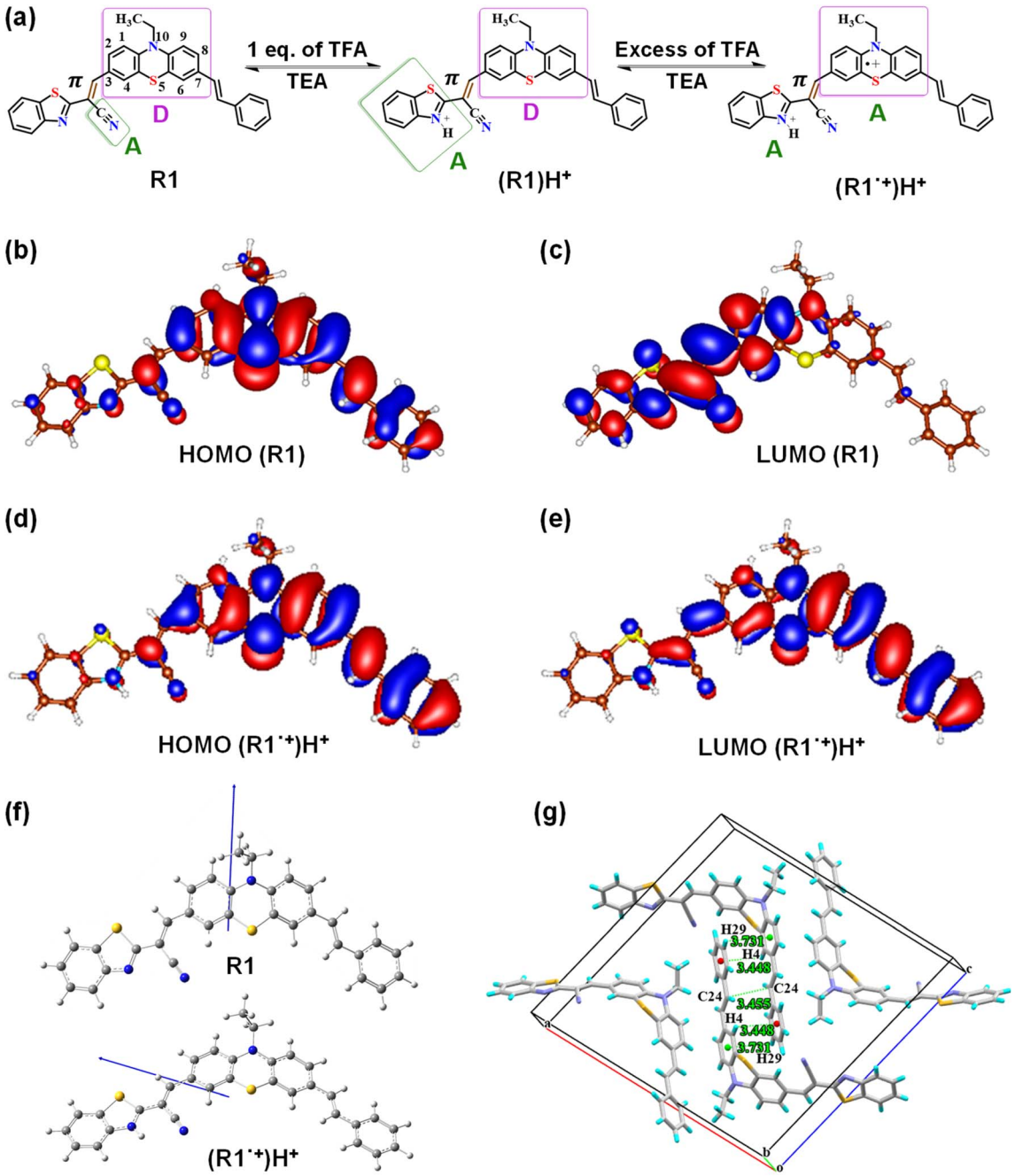

Fig. 1 The chemical structure of pristine **R1** and acid-vapor-induced cation radical formation, followed by theoretical calculation and unit cell single-crystal data. (a) Chemical structures of asymmetric (D–π–A)-type molecular system, **R1**, before and after excess protonation. Frontier molecular orbital pictures (HOMO and LUMO) of (b and c) **R1** and (d and e) $(\mathbf{R1}^{\bullet+})\mathbf{H}^{+}$. The iso-surface value used is 0.02. (f) Electric dipole moments of **R1** (7.18 debye) and $(\mathbf{R1}^{\bullet+})\mathbf{H}^{+}$ (4.18 debye). (g) Antiparallel interlayer interactions are present in the crystal lattice of **R1**. The direction of the effective electrical dipole moment for **R1** and $(\mathbf{R1}^{\bullet+})\mathbf{H}^{+}$ is shown by an arrow.

molecular frameworks showing aggregation-induced emission (AIE).[44] Electronic communication between the donor and acceptor moieties leads to intramolecular charge transfer (ICT), which modulates the energy landscapes of frontier molecular orbitals (FMOs). ICT is also responsible for the electronic polarization of 'push–pull' chromophores and generating a molecular dipole, thus accounting for enhanced optoelectronic properties. D–π–A molecules are considered potential candidates for designing organic materials displaying emission switching in response to an external stimulus.

MJs that exhibit rectifications were mainly probed in previous reports *via in situ* electrical measurements, either by conducting probe AFM, using eutectic Ga–In (EGaIn), or mechanically controllable break-junction (MC-BJ) methods. The above techniques, however, do not produce isolable MJs for large-scale production and electrical measurements that can be suitable for practical applications.

The present work describes the synthesis of a phenothiazine-based D–π–A molecular architecture with an extended π-conjugation (**R1**, Fig. 1a) that reveals a relatively lower energy band gap, red to near-infrared (NIR) emission, and acid- and base-induced reversible acidochromism in both solution and thin films, demonstrating a reconfigurable implication (popularly known as IMP) logic gate. Protonation (H^+ ions) at the acceptor site enhances its electron-accepting tendency, which further improves the charge transfer efficacy by slightly broadening the HOMO and LUMO and reducing the HOMO–LUMO gap, which may favor an improved electrical current rectification ratio.[45,46] Two-terminal (2T) electronic devices consisting of π-conjugated phenothiazine derivative films of an optimized thickness ≈58 nm in vertically stacked p^+-Si/$\mathbf{R1}_{58\ nm}$/ITO configuration were fabricated to study the charge transport phenomena by exposure to excess trifluoroacetic acid (TFA) vapors, leading to formation of cation radicals $(\mathbf{R1}^{\bullet+})\mathbf{H}^+$ and without acid vapor (**R1**). The electrical conduction of the devices increases in forward bias after 60 seconds of TFA exposure. In contrast, conduction remains unaffected under the reverse bias polarity compared to the pristine junction, resulting in a rectification ratio with nearly a 530% increment. The structural, chemical, and electrical properties were partially restored using triethylamine (TEA) vapors. The decrease in electrical resistance of the devices after acid-vapor exposure is confirmed using electrical impedance spectrum (EIS) analysis. Alternating current (AC) to direct current (DC) conversion was investigated at different frequencies, exhibiting optimum conversion at 500 Hz. The present work creates an opportunity to modulate electronic functions using small organic molecules displaying reversible fluorochromic changes in response to acid and base vapor, optoelectronic devices, and paper-based sensing applications.

Results and discussion

Design, synthesis, and characterization

Introducing molecular asymmetry is one of the important design strategies for achieving electrical current rectification in a MJ. A recent study has also shown that efficient intermolecular charge transfer between the donor and acceptor units can enhance the electrical current rectification ratio.[47] Herein, we have designed an asymmetric D–π–A molecular system (**R1**) for stimuli-responsive reversible fluorescence phenomena and enhanced rectification features. The idea was to introduce molecular asymmetry and to fine-tune the rectification by altering the HOMO–LUMO gap before and after protonation at the acceptor site. A phenothiazine (PTZ) moiety with extended π-electron conjugation acts as an electron donor. A 2-benzothiazole acetonitrile group was appended to the phenothiazine moiety through a π-spacer at the C-3 position and styrene moiety was introduced at the C-7 position of phenothiazine (Fig. 1a). The nitrile group acts as an electron acceptor under unprotonated conditions. However, upon exposure to an acid (trifluoroacetic acid, TFA) vapor, protonation occurs on nitrogen of the benzothiazole moiety, which becomes a stronger electron acceptor than the nitrile group. As a result, intramolecular charge transfer occurs from the PTZ donor to the protonated benzothiazole unit ($\mathbf{R1H}^+$, Fig. 1a). Therefore, in the same molecule, we can modulate the flow of charge carriers from the donor to different acceptors under different chemical inputs (Fig. 1a). We first conducted computational studies to confirm our hypothesis, and the results are discussed in Section S2. Density functional theory (DFT) calculations confirmed that the protonation of benzothiazole nitrogen is energetically more feasible than that at other protonation sites available in the **R1** molecule (Fig. S1). The optimized structures of **R1** and protonated $\mathbf{R1H}^+$ are illustrated in Fig. S2a and b. An electrostatic potential (ESP) map also corroborated that protonation occurs on the benzothiazole ring nitrogen of the acceptor side when **R1** is exposed to acid vapors (Fig. S2c and d). The frontier molecular orbitals (HOMO and LUMO) are depicted in Fig. 1b and c for **R1**. Energies from HOMO−9 to LUMO+9 and the HOMO and LUMO gaps for **R1** and $\mathbf{R1H}^+$ are tabulated in Table S1. The HOMOs are localized over the donor moiety, while the LUMOs are localized on the acceptor side, a desirable characteristic for exhibiting excellent electrical current rectification (Fig. S2e and f). The theoretical studies revealed that $\mathbf{R1H}^+$ exhibits a dipole moment of 14.07 debye (Fig. S2g), approximately two times higher than that of **R1** (7.18 debye). This change in dipole moment suggests a change in the electronic features of the molecule.[48]

Encouraged by the above theoretical findings, a phenothiazine-based π-extended red/near-infrared emitting dye was synthesized in 80% yield by the Knoevenagel condensation reaction between (*E*)-10-ethyl-7-styryl-10*H*-phenothiazine-3-carbaldehyde (**SPTZ**) and 2-(benzo[*d*]thiazol-2-yl) acetonitrile in ethanol by following the synthetic route as described in Scheme S1 (Section S3).[49] The compound **R1** was characterized by NMR, mass, and FT-IR spectroscopic techniques (Section S4 and Fig. S4–S8). To get an insight into the structural alterations brought about by the addition of TFA, followed by subsequent TEA addition in the **R1** molecule, ^{1}H NMR spectroscopic studies were conducted, which indicated the protonation of nitrogen present on the benzothiazole ring by TFA and its subsequent deprotonation upon exposure to TEA vapors (Section S5 and Fig. S9–S11). Interestingly, a broadening of NMR signals of **R1** was observed

upon addition of an excess of TFA (3 equiv. onwards), which was attributed to the formation of phenothiazine cation radical, $(\mathbf{R1}^{\bullet+})\mathbf{H}^{+}$, through oxidation by excess TFA (Fig. 1a). A similar observation was made experimentally by the Bunz and Viglianisi research groups.[50,51] The EPR studies of **R1** exposed to an excess of TFA also confirmed the formation of the phenothiazine cation radical in both solution and solid states (Fig. S12 and S13). The mechanism of the reaction of **R1** with TFA and subsequently added TEA is shown in Scheme S2. The optimized structure of $(\mathbf{R1}^{\bullet+})\mathbf{H}^{+}$ and the ESP mapped on the electron density surface are shown in Fig. S3b. The frontier molecular orbitals (HOMO and LUMO) are depicted for $(\mathbf{R1}^{\bullet+})\mathbf{H}^{+}$ and are shown in Fig. 1d and e. Theoretical studies revealed that the electrical dipole moment of cation radical, $(\mathbf{R1}^{\bullet+})\mathbf{H}^{+}$, is 4.18 debye, which is much lower than those predicted for either **R1** or $\mathbf{R1H}^{+}$ (Fig. 1f & S2g). This change in dipole moment corresponds to the formation of the phenothiazine cation radical in the presence of an excess of TFA that reduces the electric dipole moment. The HOMO and LUMO energies and band gaps for **R1** and $(\mathbf{R1}^{\bullet+})\mathbf{H}^{+}$ are given in Table S2. Furthermore, *N*-ethyl carbazole was synthesized as a control for device studies and characterized by ^{1}H NMR and ^{13}C NMR (Section S6, Scheme S3, and Fig. S14 and S15).

The solid-state structure of **R1** was also confirmed by single-crystal X-ray diffraction analysis (CCDC no. 2301361, see Section S7 and Fig. S16a for further discussion). The crystal system and space group of **R1** were monoclinic and $P2_1/c$, respectively (Table S3). The vinylic substituents at positions C3 and C10 are in *trans* conformation (*E*-isomer) with dihedral angles (θ_D) of 169.84° and 176.73° along the C2–C3–C25–C30 and C9–C10–C16–N3 planes, respectively (Fig. S16b). The phenothiazine unit has a highly bent butterfly-type arrangement with a dihedral angle (θ_D) of 131.66° along the C7–N1–S1–C5 plane (Fig. S16b). The planes passing through phenothiazine benzene rings make an angle of 129.1° (Fig. S16c). The π electron clouds are at a distance of 4.177 Å, affording an antiparallel herringbone arrangement (J-type) without π–π stacking (Fig. S16d); thus, it might have a reasonably high hole and electron carrier mobility.[52,53] Several other intermolecular interactions, such as N···H–C, C···H–C, S···H–C, C···C–H, S···C–C and π···H–C, were also observed (Fig. 1g, S16e and Table S4).

Thermogravimetric analysis (TGA) and differential thermal analysis (DTA) studies reveal good thermal stability of **R1**, with a 5% weight loss at a decomposition temperature of 229 °C. Thus, **R1** can tolerate thermal treatment during device fabrication (Section S8 and Fig. S17). The photophysical properties of the compound were also studied and analyzed in both solution and solid states (see SI, Section S9). **R1** displayed positive solvatochromism and a band gap of 2.17 eV ($\lambda_{em} = 632$ nm and $\Phi_{fl} = 4.5\%$) in the solid state (Fig. S18, S19 and Tables S5–S8). Furthermore, aggregation-induced emission enhancement (AIEE) behavior was also observed (see Section S10, Fig. S20 and Table S9).

Acidochromic response in solution and solid states

Inspired by computational studies on acid-induced changes in the electronic properties of pristine **R1**, we investigated the acidochromic response of **R1** through spectrophotometric titrations carried out using organic trifluoroacetic acid (TFA, $pK_a = 0.23$ at room temperature) in chloroform solution (10 μM) (Fig. S21). Detailed studies are mentioned in Section S11. Upon adding 0.11 M TFA solution, the absorption maxima band of **R1** centred at 490 nm quenches along with the gradual appearance of a new band at 648 nm (Fig. S21a and b). Thus, a bathochromic shift of 158 nm resulted due to the formation of phenothiazine cation radical $(\mathbf{R1}^{\bullet+})\mathbf{H}^{+}$ in the presence of excess TFA with a significant color change.[40] An electronic transition in $(\mathbf{R1}^{\bullet+})\mathbf{H}^{+}$ originates due to the intraligand charge transfer (ILCT) band at a lower energy. The protonated solution showed excellent chemical structural reversibility in response to triethylamine (TEA), a weak base, as ensured by UV-vis absorption spectroscopy (Fig. 2a). Furthermore, the fluorescence signal centered at 655 nm showed quenching in emission intensity upon adding nearly 47 mM of TFA solutions, indicating the high sensitivity of **R1** in the excited state compared to the ground state (Fig. 2b and S21c). Upon subsequent treatment with TEA, the emission spectrum was completely recovered to the pristine state (Fig. 2c). The optical band gaps of the pristine compound (**R1**) and cation radical $(\mathbf{R1}^{\bullet+})\mathbf{H}^{+}$ were estimated at 2.11 eV and 1.51 eV, respectively (Table S10 and Fig. S21a). The as-synthesized solid compound (powder form, **R1**) was also found to be sensitive to TFA vapors, as visual color changes can be observed by the naked eye under daylight and 365 nm wavelength of light (Fig. 2d). The emission wavelength of protonated form, $(\mathbf{R1}^{\bullet+})\mathbf{H}^{+}$, showed a 14 nm blue shift compared to pristine **R1** (632 nm for pristine **R1** to 618 nm for $(\mathbf{R1}^{\bullet+})\mathbf{H}^{+}$) along with a reduction in emission intensity (Fig. 2e). Upon treatment with TEA, the emission intensity was partially restored. The cation radical, $(\mathbf{R1}^{\bullet+})\mathbf{H}^{+}$, showed a relatively lower band gap at 1.50 eV ($\lambda_{abs} = 589$ nm) compared to pristine **R1**, which showed a band gap at 2.17 eV (Fig. S22 and Table S11). The bathochromic shift in absorption wavelengths in both solution and solid states indicates protonation-induced enhancement in the extent of charge transfer from the donor phenothiazine moiety to the acceptor,[54] as shown in Fig. 1a. As a result, the HOMO–LUMO energy gaps of protonated cation radical species $(\mathbf{R1}^{\bullet+})\mathbf{H}^{+}$ were found to be lower as compared to that of the pristine compound, **R1**.

Integration of logic gates based on acidochromic response

The acidochromic "on–off–on" response of **R1** upon subsequent addition of TFA and TEA was used to construct an IMP molecular logic gate or memristive switches[55,56] which can perform 'stateful' functions based on emission signals observed from PET mechanisms (Fig. 2f). Previous work by Uchiyama, de Silva, McCoy, and Magri motivated us to integrate logic gates based on chemical inputs and photoluminescence as output. For instance, TFA and TEA are considered two inputs, and the emissive state is assigned as '1', whereas the turn-off state is '0'. The emission spectra were recorded at room temperature (25 °C) using an excitation wavelength of 490 nm and a slit width of 5 nm. The initial emission output of **R1** in a 10 μM chloroform solution appears at 655 nm with a normalized emission

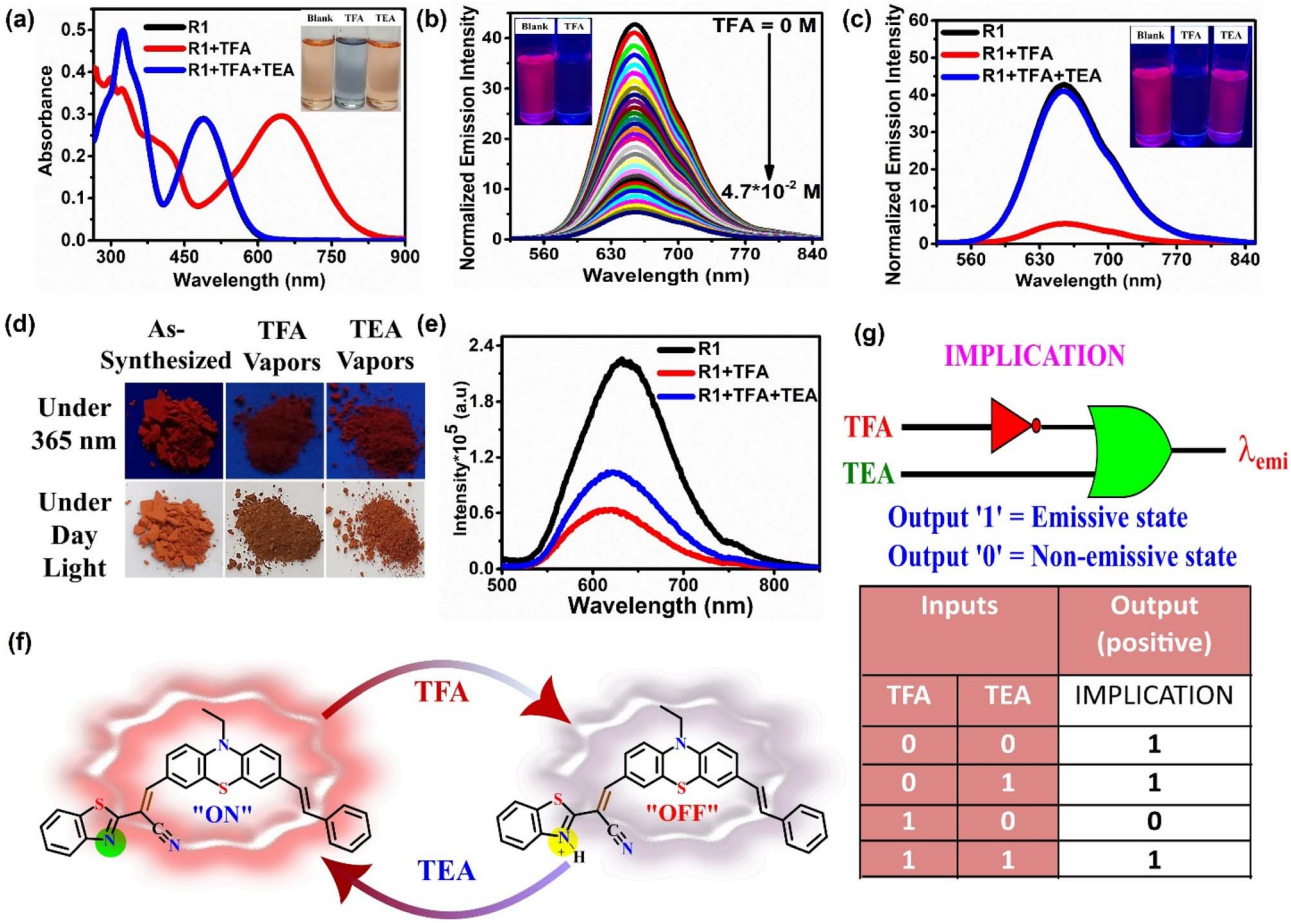

Inputs		Output (positive)
TFA	TEA	IMPLICATION
0	0	1
0	1	1
1	0	0
1	1	1

Fig. 2 UV-Vis and fluorescence studies evidence a reversible change in the R1 system upon protonation–deprotonation, followed by demonstration of the IMP molecular logic gate. (a) Absorbance reversibility spectra of R1 in chloroform (10 μM) upon sequential addition of TFA and TEA (inset shows photographs obtained under daylight), (b) fluorescence spectra of R1 in chloroform (10 μM) upon sequential addition of TFA and TEA (λ_{exci} = 490 nm, slit width = 5 nm, at 25 °C) (inset shows photographs obtained under 365 nm light), (c) emission of R1 in chloroform (10 μM) upon sequential addition of TFA and TEA, (d) photographs of powder R1 upon addition of TFA and subsequent exposure to excess TEA vapors under 365 nm light and daylight, (e) solid-state fluorescence spectra of R1 upon exposure to excess TFA and subsequent exposure to TEA vapors, (f) pictorial representation of reversible acidochromism, and (g) IMP logic gate and truth table. TFA stands for trifluoroacetic acid, and TEA indicates triethylamine.

intensity of 1.0. In the presence of input, TFA (47 mM), the emission intensity reduces to 0.12 (normalized value).

Based on the spectroscopic investigation (Fig. S23), we considered the threshold emission intensity at 0.23 (normalized value), and the intensity below this value is considered output '0' and above is marked as '1'. Without the addition of both inputs (TFA and TEA), **R1** is emissive, with the output being '1'. The output was also observed when adding TEA (input 2) only. The addition of TFA (input 1) quenches the emission, leading to output '0', and the simultaneous addition of both inputs leads to an output '1' (see the truth table in Fig. 2g). Thus, an IMPLICATION (IMP)-type logic gate was integrated, which reveals that the phenothiazine derivative holds potential in stimuli-responsive sensing for nanoelectronic applications.

Electrochemical properties of R1 and $(R1^{\bullet+})H^+$

The electrochemical features of the pristine compound and the cation radical were investigated by cyclic voltammogram (CV). **R1** exhibits a first oxidation peak at +0.40 V *vs.* $Ag/AgNO_3$, which shifts to +0.43 V *vs.* $Ag/AgNO_3$ after forming protonated $(R1^{\bullet+})H^+$ in response to TFA. The energy of the HOMO was estimated at −4.98 eV and −5.00 eV for **R1** and $(R1^{\bullet+})H^+$, respectively (Fig. S24, Section S12 and Table S12). The energy of the LUMO was estimated at −2.81 eV and −3.49 eV for **R1** and $(R1^{\bullet+})H^+$, respectively, which matches well with that of similar reported compounds. The energy gap between the HOMO–LUMO was estimated at 2.17 eV and 1.51 eV for **R1** and $(R1^{\bullet+})H^+$, respectively. Computational studies suggest that the HOMO–LUMO gap for **R1** and $(R1^{\bullet+})H^+$ is 3.05 eV and 1.43 eV, which are close to the experimental findings. The addition of TFA to **R1** not only lowers the energy of the HOMO and LUMO but also decreases the energy gap between the HOMO–LUMO. Upon the addition of TFA, the oxidation potential remains nearly unchanged, while the reduction potential shifts toward a lower potential. With the increased TFA concentration (200 μL), the potential of redox signals did not change significantly (Fig. S24c and d). This

observation also supports that protonation occurs on the nitrogen center of the benzothiazole ring.

Preparation of thin films and characterization

To explore the electrical properties and charge transport phenomena in the π-conjugated phenothiazine derivative and its protonated form, two-terminal (2T) electronic devices were fabricated with vertical stacking of p^+-Si/**R1**/ITO and p^+-Si/(**R1**$^{\bullet+}$)**H**$^+$/ITO for the pristine and protonated devices, respectively (device fabrication steps are described in Section S13). A thin film of **R1** was prepared on p^+-Si substrates. The average thickness of the film was estimated at around 58 nm, as measured from FE-SEM cross-sectional images (Fig. S25). The XPS spectra exhibit an N 1s signal at 399.34 eV for **R1** and 399.60 eV for (**R1**$^{\bullet+}$)**H**$^+$, demonstrating a shift in the binding energy of ~0.3 eV, which ensures N^+–H bond formation in (**R1**$^{\bullet+}$)**H**$^+$ (Fig. S26).

Two-terminal device fabrication and electrical characterization

A thin film of **R1** was prepared on a highly doped (p-doping, boron) Si substrate (device active area = 1.5 cm × 1.5 cm, orientation ⟨100⟩, resistivity ~ 0–100 Ω cm, and thickness 430 μm) by treating with O_2 plasma at 80 W for 10 minutes to make the Si surface hydrophilic and organic residue free. A solution of **R1** (2 mg mL^{-1} in an ethanol + chloroform mixture (1 : 1; v/v), degassed with N_2) was spin-coated on a freshly cleaned p^+-Si substrate (1500 rpm for 40 s), followed by drying in a vacuum desiccator for 2 hours. Two-terminal electronic devices were fabricated by depositing indium tin oxide (ITO) of thickness 100 ± 5 nm by the Ar sputtering method (45 minutes, 30 W, 15 standard cubic centimeters per minute, 20 rpm, 1.76 × 10^{-3} mbar vacuum pressure) using a custom-designed shadow mask.

The direct current (DC)-based electrical measurements, current–voltage studies, were performed under two different

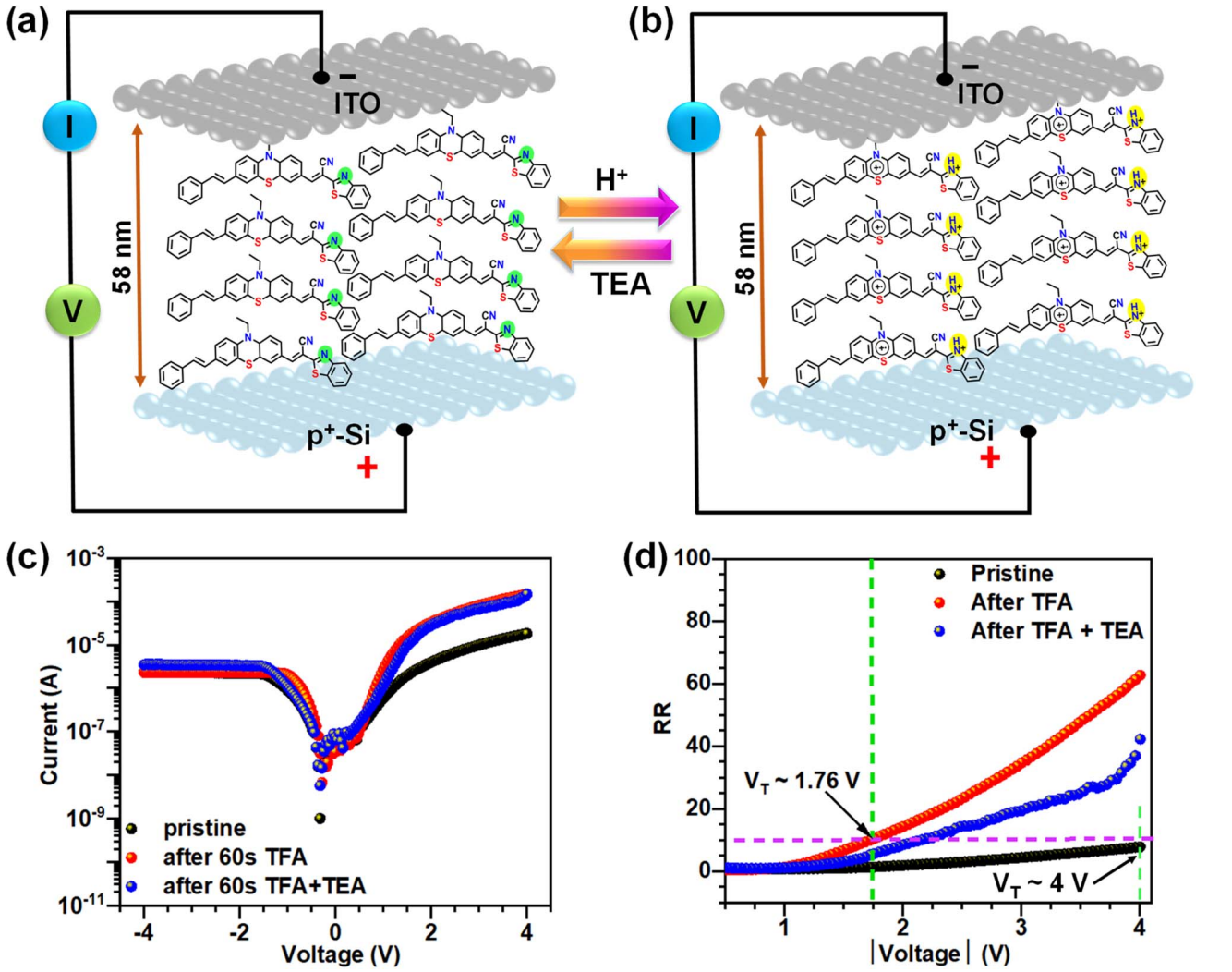

Fig. 3 Schematic illustration of 58 nm thick stacked molecular layers in a two-terminal vertical device configuration for acid and base vapor-induced DC-based electrical measurements. (a) The device stacking of p^+-Si/$R1_{58\ nm}$/ITO and (b) p^+-Si/(**R1**$^{\bullet+}$)H^+/ITO, (c) semi-logarithmic current–voltage plots measured for pristine, acid solution vapor, and triethylamine vapor, and (d) plots of the rectification ratio as a function of applied voltages (V_T, defined as the voltage at which the RR is 10; for the pristine device it is +4 V and for the acid-exposed device it is +1.76 V).

conditions. Firstly, p^+-Si was connected to the positive polarity and ITO to the negative polarity of the source meter. Secondly, the connection of p^+-Si was made negative, and ITO was positively connected. The schemes for the device measurements with **R1** and $(\mathbf{R1}^{\bullet+})\mathbf{H}^+$ are illustrated in Fig. 3a and b. The two-probe electrical measurement setup and optical images of the devices recorded under different chemical stimuli are depicted in Fig. S27. Comparison plots of semi-logarithmic current–voltage (I–V) characteristics were recorded for **R1** and $(\mathbf{R1}^{\bullet+})\mathbf{H}^+$, after adding trifluoroacetic acid + triethylamine (60 s exposure) (Fig. 3c). The average I–V curves for the pristine device, trifluoroacetic acid, and triethylamine exposed reference p^+-Si/ITO and p^+-Si/**R1**/ITO molecular junctions are presented in Fig. S28 and S29, respectively. The pristine device, p^+-Si/**R1**/ITO, displays an electrical current of 1.82×10^{-5} Amp at +4 V when p^+-Si was connected to the positive probe and 1.79×10^{-5} Amp at −4 V when p^+-Si was connected to the negative probe of the source meter. Upon exposure to acid vapor, the asymmetric I–V nature of the device showed enhancement by one order of magnitude compared to the **R1** device. For the observed electrical current for the device containing $(\mathbf{R1}^{\bullet+})\mathbf{H}^+$, we consider the ON current, $I_{ON} = 1.45 \times 10^{-4}$ Amp, at +4 V when p^+-Si was connected to the positive probe and 1.21×10^{-4} Amp at −4 V when p^+-Si was connected to the negative probe of the source meter. The increment of current was observed in one direction only, while the OFF current, I_{OFF}, remains almost constant after exposure to acid vapor ($I_{OFF} = 2.33 \times 10^{-6}$ Amp at −4 V and 2.37×10^{-6} Amp at +4 V for $(\mathbf{R1}^{\bullet+})\mathbf{H}^+$ and $I_{OFF} = 2.35 \times 10^{-6}$ Amp at −4 V and 2.35×10^{-6} Amp at +4 V for pristine conditions (**R1**)). Electrical behavior shows that acid vapor enhances the rectification behavior of the device. The electrical current rectification ratio, RR, can be defined as $\left|\frac{I(+V)}{I(-V)}\right|$, which is nearly 10 for **R1**, but upon forming cation radical, $(\mathbf{R1}^{\bullet+})\mathbf{H}^+$, it reaches 63, showing a giant enhancement of 530% in the RR. We consider a threshold voltage, V_T, defined as the voltage at which the RR is 10. For the pristine device, p^+-Si/**R1**/ITO, it is +4 V, and for the acid-exposed device it is +1.76 V. To reconfigure the device after the acid vapor exposure, we added triethylamine, which partially brings back the electrical features of the devices (Fig. 3d). Our observation ensures that the rectification originates from $(\mathbf{R1}^{\bullet+})\mathbf{H}^+$.

Electrical impedance spectra of molecular junctions

It is known that DC-based electrical measurement cannot separate the individual electrical parameters; rather, it produces a total current across the device in response to an external bias.[57,58] Frequency-dependent electrical response is crucial to investigate charge transfer resistance and other electrical parameters.[18,59] We recorded electrical impedance spectra (EIS) on two-terminal molecular junctions before and after the acid vapor exposure in the frequency range of 0.1 Hz to 5×10^6 Hz. The Nyquist plot, which depicts the imaginary impedance *vs.* real impedance ($-Z''$ *vs.* Z'), shows a depressed semicircle related to the charge transfer resistance (R_{ct}) of the device, which, after exposure to the acid vapor, reduces significantly (Fig. S30a and b). A summary of the electrical parameters is provided in Table S13. The Bode plot illustrates that both **R1** and $(\mathbf{R1}^{\bullet+})\mathbf{H}^+$ molecular devices behave as resistors at very low frequencies but act as capacitors at higher frequencies (Fig. S30c and d). The capacitive reactance $\left(X_C = \frac{1}{j\omega CPE}\right)$ indicates the resistance of a capacitor, which is a frequency-dependent quantity.[60]

Charge conduction mechanism at the molecular level

To understand the charge conduction mechanism in the **R1**-based device, electrical current was recorded at 0 to +4 V or 0 to −4 V for both polarities of the p^+ silicon electrode connected to the source meter. Subsequently, the I–V data were fitted following the space charge limited current (SCLC) conduction model that follows a well-known equation, $I \propto V^m$, where 'm' is the slope of the I–V plot. Depending on the fitted value of 'm', the charge conduction model can be predicted. For instance, the plot of $\ln(I)$ *vs.* $\ln(V)$ can be divided into three regions, which are given in the SI (Fig. S31a and b). The regions that exhibit 'm' > 2 are considered to have trap-filled charge conduction, while 'm' ∼ 2 indicates SCLC conduction. The nonlinear behavior of $\ln(I)$ *vs.* $V^{1/2}$ curves implies that the charge conduction is not controlled by Schottky emission (Fig. S31c and d). The temperature dependence of the current–voltage characteristics of p^+-Si/$(\mathbf{R1}^{\bullet+})\mathbf{H}^+$/ITO molecular junctions depicts a thermally activated hopping mechanism for long-range charge conduction (Fig. S32). The activation energy, E_a, was found to be increased to 121.24 meV measured at ±0.5 V from 90.23 meV recorded at ±0.25 V. This observation correlates the RR values, as the rectification ratio is relatively higher at ±0.5 V as compared to ±0.25 V. The activation energy at positive voltage (forward bias) is higher than that at negative voltage (reverse bias). The higher activation energy at forward bias is attributed to charge transport *via* a hopping mechanism.[1,10,17,24,59]

Testing the diode behavior of the junctions

The electrical current rectification property, RR, of any electronic device, can be well realized by checking its efficacy of alternating current (AC) to direct current (DC) conversion.[29,30,61,62] We have performed AC to DC conversion efficacy of the pristine devices after exposure to acid vapor and adding triethylamine to reconfigure the electronic properties. An oscilloscope was used for AC to DC conversion studies under two different measurement conditions. A measurement setup for AC to DC signal conversion with different connectivities of AC input signals is shown in Fig. S33a and b. Firstly, we provided the AC input signal (I/P) to the bottom electrode of the devices (p^+-Si), for both the **R1** and $(\mathbf{R1}^{\bullet+})\mathbf{H}^+$ containing devices but individually (Fig. 4a and b), and secondly, to the top electrode, *i.e.*, ITO. The output (O/P) signal was collected across a 10 kHz series resistance for both cases. Such a resistor inhibits high current flow through the circuit and thus prevents the breakdown of the devices.[62]

An AC signal of peak-to-zero amplitude ($V_{A|peak\text{-}to\text{-}zero}$) and 10 V ($V_{A|DC} = 3.18$ V) was provided as input within the frequency

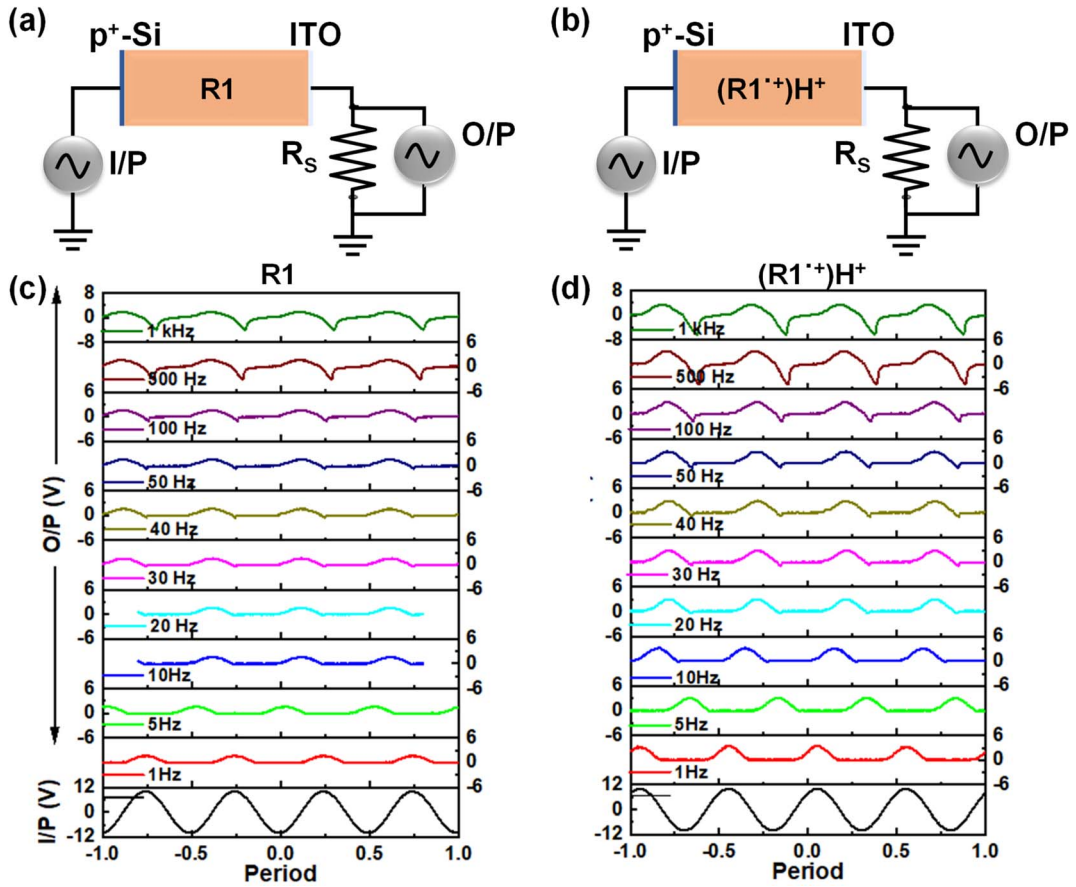

Fig. 4 Investigation of alternating current to direct current conversion efficiency. (a) A measurement setup for AC to DC signal conversion for **R1** and (b) **(R1$^{\bullet+}$)H$^+$**. (c) Conversion of AC to DC signals of p$^+$-Si/**R1**$_{58\ nm}$/ITO and (d) p$^+$-Si/**(R1$^{\bullet+}$)H$^+$**$_{58\ nm}$/ITO after 60 s of exposure. The data were collected at different frequencies (minimum 1 Hz and maximum 1 kHz).

range of 1 Hz to 1 kHz. The **R1**-containing device acts as a poor DC converter, passing only the negative polarity of the signal with $V_{A|peak\text{-}to\text{-}zero}$ (O/P) ~ 1.64 V ($V_{A|DC}$ = 0.52 V). In response to acid vapor, the DC conversion enhances significantly ($V_{A|peak\text{-}to\text{-}zero}$ (O/P) ~ 3.4 V ($V_{A|DC}$ = 1.08 V)) (Fig. 4c and d), following an identical behavior to that observed with DC-based *I–V* measurements. Enhanced AC to DC conversion was also observed when the AC input signal was provided to the ITO contact (Fig. S34). The AC to DC conversion observed under both measurement conditions strongly supports the origin of rectification as a molecular property. Control device experiments with p$^+$-Si/carbazole/ITO and p$^+$-Si/*N*-ethylcarbazole/ITO configurations also demonstrated the acid-induced changes in the device characteristics. For p$^+$-Si/carbazole/ITO devices, the pristine films showcased a maximum RR of ~170 at ±2.5 V, which decreased to ~80 after exposure to acid vapor (Section S14, Fig. S35 and S36). However, p$^+$-Si/*N*-ethylcarbazole/ITO molecular junctions displayed the RR almost constant at lower bias ±0.5 V, decreased at ±1 V to ±3 V and increased at the ±3 V to ±4 V potential window as compared to pristine ethylcarbazole films (Fig. S37 and S38). These experiments suggest that the RR entirely depends upon the nature of the molecule and alignment of molecular orbitals with respect to the Fermi energy level of the electrodes in the presence and absence of external stimuli such as acid and base vapours utilized in this work.

Theoretical transport model of the molecular junctions

For theoretical studies, **R1** and **R1H$^+$** are considered rather than the complex structure of **(R1$^{\bullet+}$)H$^+$**. This simplification was made to avoid the use of complicated and expensive calculations. We aim to consider one equivalent of protonation to **R1** for the theoretical calculation. We consider the thermally activated hopping transport inside the oligomer film, as the charge carriers within the thicker (~58 nm) molecular thin films can't tunnel. According to Marcus' theory,[61] the charge hopping rate, k_h, can be estimated from eqn (i):

Table 1 Hopping integrals *J*, reorganization energies λ, and charge hopping rates k_h for **R1** and **R1H$^+$** calculated at T = 300 K

		Electrons		Holes	
Entities	λ, eV	*J*, meV	k_h, ps^{-1}	*J*, eV	k_h, ps^{-1}
R1	0.12	2.1	0.010	42.1	4.7
R1H$^+$	0.13	1.5	0.005	35.4	2.6

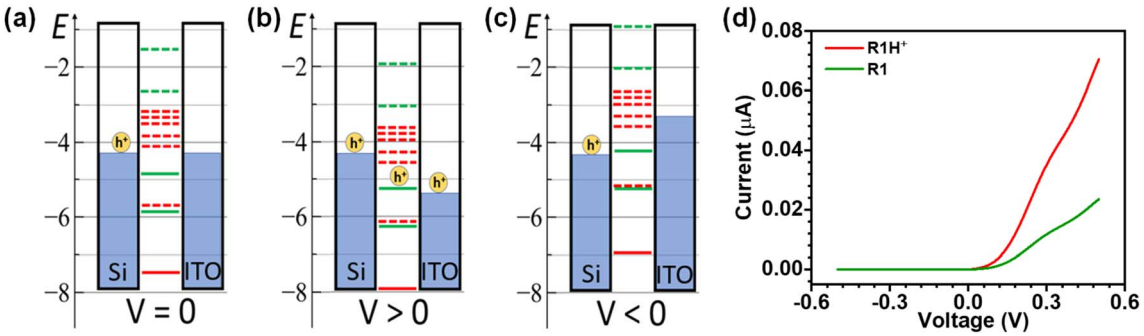

Fig. 5 Schematic representation of the hole transfer through **R1** (green) and **R1H**$^+$ (red). Solid and dashed lines represent occupied and unoccupied molecular levels, respectively, calculated at the PBE/cc-pvdz level of theory. Illustration of charge conduction in an MJ when the Si electrode is considered grounded at (a) $V = 0$, (b) $V > 0$, and (c) $V < 0$, and (d) the resulting schematic asymmetric I–V characteristic. All data in the figure are the results of calculations rather than experiments.

$$k_h = \frac{2\pi}{\hbar} J^2 \frac{1}{\sqrt{4\pi k T \lambda}} \exp\left(-\frac{\lambda}{4kT}\right) \quad \text{(i)}$$

Here, J is the hopping integral relevant to intermolecular electronic coupling and λ represents the reorganization energy. Both J and λ parameters characterize the hopping conductivity of the organic film. The reorganization of energy is relevant to the change of the molecular structure due to additional charge, and J is relevant to intermolecular coupling. However, calculations of the hopping integral J are somewhat trickier. It characterizes intermolecular coupling and therefore depends strongly on the relative position of two molecules. Since we deal with an amorphous film, different relative positions can appear. However, considering the short-range ordering, we extract the approximate positions of the adjacent molecules from the experimentally obtained crystal structure of **R1** (Section S15 and Fig. S39). Calculated values for λ, J, and k_h are presented in Table 1, and corresponding computational details are provided in the SI file.

Both **R1** and **R1H**$^+$ reveal similar hopping rates. Therefore, the difference between their conductivities is only due to the charge carriers' injection process. However, there is a strong asymmetry between electron and hole transport: the hole mobility is about 500 times higher than that for electrons. This fact can partially explain the experimentally observed rectification behavior: holes can easily transfer through the polymer from the hole-rich silicon to the ITO lead.

Band diagram model

The origin of rectification in the phenothiazine-based molecule (**R1**) in response to the acid vapor can be explained through a band diagram model. Though intrinsically Si and ITO are semiconductors, due to high doping, their carrier concentration is large (low resistivity ~ few ohms). So, the electrode materials can be treated as metals in the context of the charge conduction model, as reported earlier with organic electronic devices.[62–66] Their Fermi level is about −4.5 eV with respect to the vacuum level. The schematic representation of asymmetric I–V characteristics is illustrated in Fig. 5. At the applied voltage $V > 0$, the HOMO level of **R1** or LUMO and a set of higher levels of **R1H**$^+$ are suitable for hole transport. At voltage $V < 0$, the reverse current from ITO to Si is suppressed due to the low hole concentration in ITO. Better conductivity of the **R1H**$^+$s is explained by the presence of more transport levels.

Concluding remarks

Designing and achieving molecular rectification has been a longstanding goal of scientific communities. Following the well-established strategy of introducing molecular asymmetry to achieve molecular rectification, we have synthesized a red-emitting π-conjugated phenothiazine-based D–π–A molecule and fine-tuned its rectification behavior by altering the HOMO–LUMO gap and dipole moment through protonation at the acceptor site. Protonation reduced the HOMO–LUMO gap from 2.17 eV (**R1**) to 1.51 eV (**R1**$^{\bullet+}$)**H**$^+$. Reversible fluorochromic switching in response to TFA and TEA vapors was used to create an IMPLICATION-type logic gate. This motivated us to design and fabricate nanoelectronic devices that can alter the electronic functions in response to external stimuli. The DFT-based calculations indicate that in (**R1**$^{\bullet+}$)**H**$^+$, the HOMO–LUMO gap decreases (1.43 eV for (**R1**$^{\bullet+}$)**H**$^+$ *vs.* 3.05 eV for **R1**), suggesting a higher transmission probablity, which is consistent with our experimental observations. A change in the energy landscape of frontier molecular orbitals before and after exposure to the acid vapor induces the rectification functionality.

Our work aims to fill this gap by combining a simple chemical approach and two-terminal device fabrication. For the pristine device, the rectification ratio of 10 was tuned to 530% just by introducing acid vapor for 60 seconds. Interestingly, the device was able to partially reconfigure its chemical and electronic properties in response to triethylamine vapor. Tailorable molecular devices in response to external stimuli are highly beneficial in mimicking CMOS electronics. Both the DC and AC-based diode behaviors equivocally support the fact that the origin of rectification is certainly molecular in nature. Our devices reveal AC to DC conversion efficacy at a frequency of 500 Hz, which is a strong signature of diode behavior. Our method of device fabrication is also viable and versatile. We found that nearly 86% of devices show reproducible diode functionalities (18 molecular junctions out of 21 molecular junctions tested for this study).

Overall, we have demonstrated that exposing a molecular junction to an acid/base solution vapor can be a facile approach to regulate not only charge conduction but also the creation of new electronic functions at the molecular level. Our present study can pave the way for the development of organic molecule-based high-rectification and acid sensors.

Author contributions

R. K.: methodology; formal analysis; writing – original draft; N. P.: methodology; formal analysis; writing – original draft; R. K.: additional device fabrication; formal analysis; writing – original draft; G.: methodology; formal analysis; writing – original draft; R. S.: methodology; formal analysis; writing – original draft; D. M.: software; writing – original draft; K. K.: software, writing – original draft; P. C. M.: conceptualization; funding acquisition; resources; supervision; writing – original draft; M. D. M.: conceptualization; funding acquisition; resources; supervision; writing – original draft. All authors contributed to the discussion and editing of the manuscript.

Conflicts of interest

The authors declare that they have no known competing financial interests or personal relationships that could have appeared to influence the work reported in this paper.

Data availability

CCDC 2301361 contains the supplementary crystallographic data for this paper.[67]

The data supporting this article have been included as part of the SI. Synthesis and characterization of **R1** compound and *N*-ethyl carbazole, theoretical and experimental evidence for the site of protonation in **R1** compound, EPR studies, single crystal structure analysis, thermogravimetric analysis, photophysical properties in solution and solid state, acidochromism experiments, electrochemical measurement data, optical band gap, FESEM, XPS, EIS measurement data, electrical characterization, and computational study results are provided in the SI (PDF). See DOI: **https://doi.org/10.1039/d5sc03848k**.

Acknowledgements

R. K. acknowledges the Council for Scientific and Industrial Research (CSIR) India for Junior and Senior Research Fellowships. N. P. thanks IIT Kanpur for the institute postdoctoral fellowship (IPDF-313). R. Kaur thanks the UGC India (NTA Ref. No.: 211610012732) for a Senior Research Fellowship. Gunjan and R. S. acknowledge the University Grant Commission (UGC), India, for a research fellowship. P. C. M. acknowledges financial support from the Science and Engineering Research Board (SERB, Grant No. CRG/2022/005325) and the Ministry of Education under the Scheme for Transformational and Advanced Research in Sciences (STARS), project no. MoE-STARS/STARS-2/2023-0535, New Delhi, India. M. D. M. is grateful to the Institution of Eminence (IoE), University of Delhi, for financial support under Faculty Research Project grants (IoE/2023-24/12/FRP) and (IoE/2024-25/12/FRP). R. K., Gunjan, R. S. and M. D. M. are also grateful to the Department of Chemistry, University of Delhi, for FT-IR, TGA, absorption and fluorescence facilities and the University Science Instrumentation Centre (USIC), University of Delhi, for NMR, EPR, HRMS, Solid FL, time-resolved fluorescence, and powder X-ray diffraction facilities. The authors thank Ranjeev Kumar Parashar for growing single crystals and for data collection.

References

1 R. Gupta, J. A. Fereiro, A. Bayat, A. Pritam, M. Zharnikov and P. C. Mondal, *Nat. Rev. Chem.*, 2023, **7**, 106–122.
2 P. Sachan, A. Mahapatra, L. A. Sai Channapragada, R. Kaur, S. Sahay and P. C. Mondal, *Chem. Sci.*, 2025, **16**, 10990–11001.
3 S. Gunasekaran, D. A. Reed, D. W. Paley, A. K. Bartholomew, L. Venkataraman, M. L. Steigerwald, X. Roy and C. Nuckolls, *J. Am. Chem. Soc.*, 2020, **142**, 14924–14932.
4 T. A. Su, M. Neupane, M. L. Steigerwald, L. Venkataraman and C. Nuckolls, *Nat. Rev. Mater.*, 2016, **1**, 16002.
5 W. Haiss, C. Wang, I. Grace, A. S. Batsanov, D. J. Schiffrin, S. J. Higgins, M. R. Bryce, C. J. Lambert and R. J. Nichols, *Nat. Mater.*, 2006, **5**, 995–1002.
6 A. Vilan, D. Aswal and D. Cahen, *Chem. Rev.*, 2017, **117**, 4248–4286.
7 R. Kaur, B. Singh, V. Singh, M. Zharnikov and P. C. Mondal, *Coord. Chem. Rev.*, 2024, **514**, 215872.
8 L. Luo and C. D. Frisbie, *J. Am. Chem. Soc.*, 2010, **132**, 8854–8855.
9 C. V. S. Batista, L. Merces, C. A. R. Costa, D. H. S. Camargo and C. C. B. Bufon, *Adv. Funct. Mater.*, 2022, **32**, 2108478.
10 Z. Xie, I. Bâldea and C. D. Frisbie, *Chem. Sci.*, 2018, **9**, 4456–4467.
11 C. A. Nijhuis, W. F. Reus, A. C. Siegel and G. M. Whitesides, *J. Am. Chem. Soc.*, 2011, **133**, 15397–15411.
12 M. Carlotti, S. Soni, S. Kumar, Y. Ai, E. Sauter, M. Zharnikov and R. C. Chiechi, *Angew. Chem., Int. Ed.*, 2018, **57**, 15681–15685.
13 A. Bayat, J. C. Lacroix and R. L. McCreery, *J. Am. Chem. Soc.*, 2016, **138**, 12287–12296.
14 Q. Van Nguyen, P. Martin, D. Frath, M. L. Della Rocca, F. Lafolet, C. Barraud, P. Lafarge, V. Mukundan, D. James, R. L. McCreery and J. C. Lacroix, *J. Am. Chem. Soc.*, 2017, **139**, 11913–11922.
15 F. Y. Rahman, R. Deb, S. Sarkar, H. Banik, M. J. Uddin, S. Chakraborty, D. Bhattacharjee and S. A. Hussain, *ACS Appl. Electron. Mater.*, 2023, **5**, 3685–3697.
16 R. Kaur, A. Malik, R. Gupta, K. Kumari, S. K. Singh, P. R. Bueno and P. C. Mondal, *Chem. Sci.*, 2025, **16**, 3560–3570.
17 P. C. Mondal, U. M. Tefashe and R. L. McCreery, *J. Am. Chem. Soc.*, 2018, **140**, 7239–7247.
18 R. Gupta, P. Jash, P. Sachan, A. Bayat, V. Singh and P. C. Mondal, *Angew. Chem., Int. Ed.*, 2021, **60**, 26904–26921.
19 R. L. McCreery, *Acc. Chem. Res.*, 2022, **55**, 2766–2779.
20 A. Morteza Najarian, A. Bayat and R. L. McCreery, *J. Am. Chem. Soc.*, 2018, **140**, 1900–1909.

21 P. Gehring, J. M. Thijssen and H. S. J. van der Zant, *Nat. Rev. Phys.*, 2019, **1**, 381–396.
22 C. Jia and X. Guo, *Chem. Soc. Rev.*, 2013, **42**, 5642.
23 J. Jang, G. D. Kong and H. J. Yoon, *Acc. Mater. Res.*, 2024, **5**, 1251–1262.
24 C. Grave, C. Risko, A. Shaporenko, Y. Wang, C. Nuckolls, M. A. Ratner, M. A. Rampi and M. Zharnikov, *Adv. Funct. Mater.*, 2007, **17**, 3816–3828.
25 Y. Ai, A. Kovalchuk, X. Qiu, Y. Zhang, S. Kumar, X. Wang, M. Kühnel, K. Nørgaard and R. C. Chiechi, *Nano Lett.*, 2018, **18**, 7552–7559.
26 Y. Wang, Q. Zhang, H. P. A. G. Astier, C. Nickle, S. Soni, F. A. Alami, A. Borrini, Z. Zhang, C. Honnigfort, B. Braunschweig, A. Leoncini, D.-C. Qi, Y. Han, E. del Barco, D. Thompson and C. A. Nijhuis, *Nat. Mater.*, 2022, **21**, 1403–1411.
27 T. Ran, S. Kaplan and E. Shapiro, *Nat. Nanotechnol.*, 2009, **4**, 642–648.
28 F. Cheng, A. J. Young, J.-S. G. Bouillard, N. T. Kemp, R. Guillet-Nicolas, C. H. Hall, D. Roberts, A. H. Jaafar, A. M. Adawi, F. Kleitz, A. Imhof, M. R. Reithofer and J. M. Chin, *J. Am. Chem. Soc.*, 2019, **141**, 12989–12993.
29 J. Trasobares, D. Vuillaume, D. Théron and N. Clément, *Nat. Commun.*, 2016, **7**, 1–9.
30 H. J. Yoon, K. C. Liao, M. R. Lockett, S. W. Kwok, M. Baghbanzadeh and G. M. Whitesides, *J. Am. Chem. Soc.*, 2014, **136**, 17155–17162.
31 R. K. Parashar, P. Jash, M. Zharnikov and P. C. Mondal, *Angew. Chem., Int. Ed.*, 2024, **63**, e202317413.
32 M. Souto, V. Díez-Cabanes, L. Yuan, A. R. Kyvik, I. Ratera, C. A. Nijhuis, J. Cornil and J. Veciana, *Phys. Chem. Chem. Phys.*, 2018, **20**, 25638–25647.
33 M. Souto, L. Yuan, D. C. Morales, L. Jiang, I. Ratera, C. A. Nijhuis and J. Veciana, *J. Am. Chem. Soc.*, 2017, **139**, 4262–4265.
34 H. Atesci, V. Kaliginedi, J. A. Celis Gil, H. Ozawa, J. M. Thijssen, P. Broekmann, M. A. Haga and S. J. Van Der Molen, *Nat. Nanotechnol.*, 2018, **13**, 117–121.
35 Z. Yang, P. A. Cazade, J. L. Lin, Z. Cao, N. Chen, D. Zhang, L. Duan, C. A. Nijhuis, D. Thompson and Y. Li, *Nat. Commun.*, 2023, **14**, 5639.
36 A. Aviram and M. A. Ratner, *Chem. Phys. Lett.*, 1974, **29**, 277–283.
37 G. J. Ashwell and A. Chwialkowska, *Chem. Commun.*, 2006, 1404–1406.
38 S. Uchiyama, N. Kawai, A. P. de Silva and K. Iwai, *J. Am. Chem. Soc.*, 2004, **126**, 3032–3033.
39 M. E. S. West, C. Y. Yao, G. Melaugh, K. Kawamoto, S. Uchiyama and A. P. de Silva, *Chem.–Eur. J.*, 2021, **27**, 13268–13274.
40 A. P. de Silva and S. Uchiyama, *Top. Curr. Chem.*, 2011, **300**, 1–28.
41 A. P. de Silva, H. Q. N. Gunaratne and C. P. McCoy, *Nature*, 1993, **364**, 42–44.
42 S. Erbas-Cakmak, S. Kolemen, A. C. Sedgwick, T. Gunnlaugsson, T. D. James, J. Yoon and E. U. Akkaya, *Chem. Soc. Rev.*, 2018, **47**, 2228–2248.
43 D. C. Magri, *Coord. Chem. Rev.*, 2021, **426**, 213598.
44 L. Tu, Y. Xie, Z. Li and B. Tang, *SmartMat*, 2021, **2**, 326–346.
45 J. An, X. Luo, S. Naskar, D. Wu, C. Herrmann, J. Xia and H. Li, *J. Phys. Chem. Lett.*, 2024, **15**, 9037–9042.
46 B. Wu, W. Guo, J. An and H. Li, *J. Mater. Chem. C*, 2022, **10**, 13483–13498.
47 R. P. Sullivan, J. T. Morningstar, E. Castellanos-Trejo, R. W. Bradford, Y. J. Hofstetter, Y. Vaynzof, M. E. Welker and O. D. Jurchescu, *Sci. Adv.*, 2022, **8**, 16–18.
48 Z. A. Lamport, A. D. Broadnax, D. Harrison, K. J. Barth, L. Mendenhall, C. T. Hamilton, M. Guthold, T. Thonhauser, M. E. Welker and O. D. Jurchescu, *Sci. Rep.*, 2016, **6**, 38092.
49 J. Kumpf, S. T. Schwaebel and U. H. F. Bunz, *J. Org. Chem.*, 2015, **80**, 5159–5166.
50 M. Hauck, J. Schönhaber, A. J. Zucchero, K. I. Hardcastle, T. J. J. Müller and U. H. F. Bunz, *J. Org. Chem.*, 2007, **72**, 6714–6725.
51 R. Amorati, L. Valgimigli, A. Baschieri, Y. Guo, F. Mollica, S. Menichetti, M. Lupi and C. Viglianisi, *ChemPhysChem*, 2021, **22**, 1446–1454.
52 M. D. Curtis, J. Cao and J. W. Kampf, *J. Am. Chem. Soc.*, 2004, **126**, 4318–4328.
53 Y. Liu, Y. Guo and Y. Liu, *Small Struct.*, 2021, **2**, 2000083.
54 *Principles of Fluorescence Spectroscopy*, ed. J. R. Lakowicz, Springer US, Boston, MA, 3rd edn, 2006.
55 K. Kaniewska, P. Bollella and E. Katz, *ChemPhysChem*, 2020, **21**, 2150–2154.
56 J. Borghetti, G. S. Snider, P. J. Kuekes, J. J. Yang, D. R. Stewart and R. S. Williams, *Nature*, 2010, **464**, 873–876.
57 P. Jash, R. K. Parashar, C. Fontanesi and P. C. Mondal, *Adv. Funct. Mater.*, 2022, **32**, 2109956.
58 C. S. S. Sangeeth, A. Wan and C. A. Nijhuis, *J. Am. Chem. Soc.*, 2014, **136**, 11134–11144.
59 R. Gupta, S. Bhandari, S. Kaya, K. P. Katin and P. C. Mondal, *Nano Lett.*, 2023, **23**, 10998–11005.
60 A. J. Bard and L. R. Faulkner, *Electrochemical Methods: Fundamentals and Applications*, 2nd edn, 2001.
61 R. A. Marcus, *Angew. Chem., Int. Ed.*, 1993, **32**, 1111–1121.
62 T. Li, V. K. Bandari, M. Hantusch, J. Xin, R. Kuhrt, R. Ravishankar, L. Xu, J. Zhang, M. Knupfer, F. Zhu, D. Yan and O. G. Schmidt, *Nat. Commun.*, 2020, **11**, 3592.
63 X.-C. Fan, K. Wang, Y.-Z. Shi, Y.-C. Cheng, Y.-T. Lee, J. Yu, X.-K. Chen, C. Adachi and X.-H. Zhang, *Nat. Photonics*, 2023, **17**, 280–285.
64 J. Sun, H. Ahn, S. Kang, S.-B. Ko, D. Song, H. A. Um, S. Kim, Y. Lee, P. Jeon, S.-H. Hwang, Y. You, C. Chu and S. Kim, *Nat. Photonics*, 2022, **16**, 212–218.
65 J. Kim, D. Rhee, O. Song, M. Kim, Y. H. Kwon, D. U. Lim, I. S. Kim, V. Mazánek, L. Valdman, Z. Sofer, J. H. Cho and J. Kang, *Adv. Mater.*, 2022, **34**, 2106110.
66 S. J. He, R. White, D. K. Wang, J. Zhang, N. Jiang and Z. H. Lu, *Org. Electron.*, 2014, **15**, 3370–3374.
67 R. Kumari, N. Pal, R. Kaur, Gunjan, R. Sharma, D. Manna, K. Katin, P. C. Mondal and M. D. Milton, CCDC 2301361: Experimental Crystal Structure Determination, 2025, DOI: **10.5517/ccdc.csd.cc2h7rgz**.